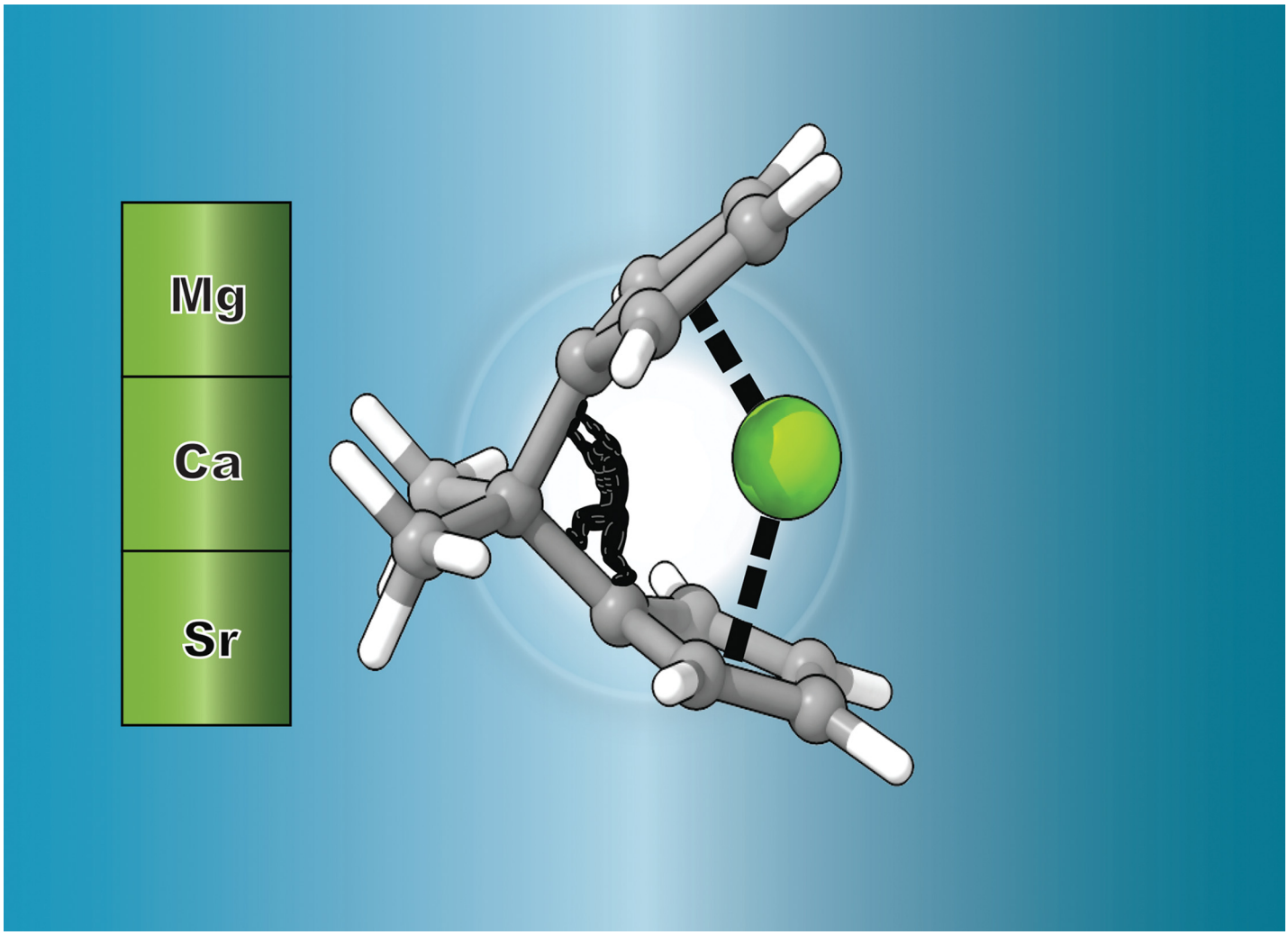

Showcasing work from the group of Professor Elfi Kraka, Computational and Theoretical Chemistry Group (CATCO), Southern Methodist University, USA.

Metal–ring interactions in group 2 *ansa*-metallocenes: assessed with the local vibrational mode theory

This work investigates group 2 *ansa*-metallocenes by analyzing 37 distinct compounds using computational and theoretical methods, notably local mode analysis. Through the intrinsic strength of the metal–cyclopentadienyl bond, structural disparities and the influence of solvation on complex stability are revealed, while the unique effects of bridging motifs are elucidated. This computational study offers valuable insights into the role of *ansa*-metallocenes in catalysis and materials science.

As featured in:

See Juliana J. Antonio and Elfi Kraka, *Phys. Chem. Chem. Phys.*, 2024, **26**, 15143.

ROYAL SOCIETY OF CHEMISTRY

rsc.li/pccp

Registered charity number: 207890

PCCP Owner Societies

PCCP

ROYAL SOCIETY OF CHEMISTRY

PAPER

View Article Online
View Journal | View Issue

Cite this: *Phys. Chem. Chem. Phys.*, 2024, **26**, 15143

Metal–ring interactions in group 2 *ansa*-metallocenes: assessed with the local vibrational mode theory†

Juliana J. Antonio and Elfi Kraka *

Ansa-metallocenes, a vital class of organometallic compounds, have attracted significant attention due to their diverse structural motifs and their pivotal roles in catalysis and materials science. We investigated 37 distinct group 2 *ansa*-metallocenes at the B3LYP-D3/def2-TZVP level of theory. Utilizing local mode force constants derived from our local vibrational mode theory, including a special force constant directly targeting the metal–ring interaction, we could unveil latent structural differences between solvated and non-solvated metallocenophanes and the influence of the solvent on complex stability and structure. We could quantify the intrinsic strength of the metal–cyclopentadienyl (M–Cp) bonds and the influence of the bridging motifs on the stiffness of the Cp–M–Cp angles, another determinant of complex stability. LMA was complemented by the analysis of electronic density, utilizing the quantum theory of atoms in molecules (QTAIM), which confirmed both the impact of solvent coordination on the strength of the M–Cp bond(s) and the influence of the bridging motif on the Cp–M–Cp angles. The specific effect of the *ansa*-motif on the M–Cp interaction was further elucidated by a comparison with linear/bent metallocene structures. In summary, our results identify the local mode analysis as an efficient tool for unraveling the intricate molecular properties of *ansa*-metallocenes and their unique structural features.

Received 18th January 2024,
Accepted 12th April 2024

DOI: 10.1039/d4cp00225c

rsc.li/pccp

Introduction

Metallocenes have received considerable attention for their varied applications in catalysis, materials science, and organic synthesis.[1–5] These sandwich-like π-complexes are typically composed of transition metal d-block elements, although s- and p-block elements can also be used.[6–9] The alteration of metallocenes to have an inter-linkage of two cyclopentadienyl (Cp) ligands forms a unique bridging motif, affecting the overall reactivity and electronic properties and resulting in so-called *ansa*-metallocenes, which are also known as metallocenophanes.[10] These compounds exhibit intriguing properties owing to the interplay between the metal center and the conjugated π-system of the cyclopentadienyl rings. A variety of transition metal *ansa*-metallocenes have emerged as promising materials of research due to their applications in olefin and ring-opening polymerizations.[11–14] As such, a comprehensive understanding of the structural, electronic, and reactivity aspects of metallocenophanes is crucial for tailoring their applications in diverse fields.

Although there have been extensive studies over the years on d-block metallocenophanes, main-group metallocenophanes are a relatively newer and less explored field. Among the main-group metallocenophanes, a majority of group 2 *ansa*-metallocenes have been synthesized and structurally/theoretically characterized, with most of the structures being magnesocenophanes and calcocenophanes.[7,15–23] For more information on synthetic routes for main-group *ansa*-metallocenes, the reader is referred to ref. 24. As mentioned previously, the defining structural motif of *ansa*-metallocenes is the inter-linkage of Cp rings, of which primarily carba- or sila-bridged motifs are utilized, and can be either one-atom-bridged [1] or two-atom-bridged [2] motifs. Magnesocenophanes have been synthesized as mainly single-atom-bridged carba- and sila-bridged components; however, carba- and sila-[2]magnesocenophanes have also been reported.[18,25] Calcocenophanes, on the other hand, are primarily two-atom-bridged carba- and sila- motifs, with a variety of substitution patterns. The primary application of group 2 metallocenophanes is for transmetalation reactions to prepare for transition metal or p-block *ansa*-metallocenophanes. Recently, however, there was a report on utilizing magnesocenophanes as catalysts for dehydrocoupling reactions of amine boranes.[15,26]

Computational and Theoretical Chemistry Group (CATCO), Department of Chemistry, Southern Methodist University, 3215 Daniel Ave, Dallas, TX 75275-0314, USA. E-mail: ekraka@smu.edu

† Electronic supplementary information (ESI) available: Cartesian coordinates of optimized structures. See DOI: https://doi.org/10.1039/d4cp00225c

Due to the poor solubility of group 2 metallocenophanes in nonpolar solvents, experimentally obtained crystal structures exhibit solvent coordination with the central metal atom, with the donor solvent being either tetrahydrofuran (THF) or dimethoxyethane (DME). Very few studies, experimental and theoretical alike, have studied the structural and electronic properties of group 2 *ansa*-metallocenes, with the majority of reports detailing synthetic routes and mechanistic studies.[15,26,27]

In this work, we have applied local mode analysis (LMA), developed in our group,[28,29] as a tool to assess the intrinsic bond strengths for 37 *ansa*-complexes (with four metallocene structures) shown in Fig. 1–3, with the aims to (i) compare the trend of bond strengths between the metals (M, where M = Mg, Ca, Sr) and Cp rings going down the group 2 periodic table, (ii) investigate the effect of M–Cp, and M–O bond strengths and Cp–M–Cp stiffness going from a non-solvated metallocenophane to a solvated metallocenophane, (iii) investigate the electronic density, and (iv) probe the effects that the bridging motifs (whether single or double and carba- or sila-bridge motifs) have on the Cp–M–Cp stiffness, and (v) compare bent with linear metallocene complexes.[30]

Computational methods

Local mode analysis theory

LMA, originally introduced by Konkoli and Cremer,[31,32] has evolved over the years into a versatile computational instrument, facilitating the extraction of critical chemical insights from vibrational spectroscopy data. LMA refines the use of normal vibrational force constants and frequencies derived from normal vibrational modes to characterize chemical bonds and/or weak chemical interactions. The normal vibrational modes of a polyatomic molecule are generally delocalized, as stated by Wilson in 1941 *via* his proof that the associated normal mode coordinates $\boldsymbol{Q}$ are a linear combination of internal coordinates $\boldsymbol{q}$ or Cartesian coordinates $\boldsymbol{x}$.[33] Therefore, normal mode stretching frequencies and associated stretching force constants are of limited use as individual bond strength descriptors. Konkoli and Cremer solved this problem by the transformation of normal vibrational modes into their local mode counterparts.[31,32] Mathematical details can be found in two comprehensive review articles.[28,29] A local vibrational mode $\boldsymbol{a}_n$ is defined as

$$\boldsymbol{a}_n = \frac{\mathbf{K}^{-1}\boldsymbol{d}_n^{\dagger}}{\boldsymbol{d}_n\mathbf{K}^{-1}\boldsymbol{d}_n^{\dagger}} \quad (1)$$

Important to note is that the two ingredients needed for LMA, the diagonal normal mode force constant matrix $\mathbf{K}$ in normal mode coordinates $\boldsymbol{Q}$ and the normal mode vectors $\boldsymbol{d}_n$ in internal coordinates, can be obtained from a vibrational frequency calculation *via* the Wilson GF formalism,[33–35] a routine part of the most modern quantum chemistry packages.[36]

The calculation of the corresponding local mode force constant k_n^a can be performed using the following expression:

$$k_n^a = \boldsymbol{a}_n^{\dagger}\mathbf{K}\boldsymbol{a}_n. \quad (2)$$

This enables the computation of the local mode frequency ω_n^a:

$$(\omega_n^a)^2 = (4\pi^2c^2)^{-1}\frac{k_n^a}{m_n^a}, \quad (3)$$

with m_n^a being the local mode mass.[31,32]

We have recently developed a unique local mode force constant between the metal and the geometric center of the ring to quantitatively describe metal–π interactions,[37] typically found in sandwich compounds[38,39] but also in transition metal catalysts[40] and enzymes as well.[41]

In this work, we utilized the local force constant between the metal and the geometric center of the Cp ring, k^a(M–Cp), and the local force constant of the angle between the two Cp rings and the metal k^a(Cp–M–Cp) as illustrated in Fig. 4.

For the magnesocenophane, calcocenophane and strontiocenophane structures with THF or DME solvent molecules attached to the metal, we have also used the local force constants k^a(Mg–O), k^a(Ca–O), and k^a(Sr–O). These local force constants were transformed into relative bond strength orders (BSOs) according to the generalized Badger rule derived by Cremer, Kraka, and coworkers[42,43] *via* a power relationship in the form of BSO = $A(k^a)^B$. Two reference molecules with known

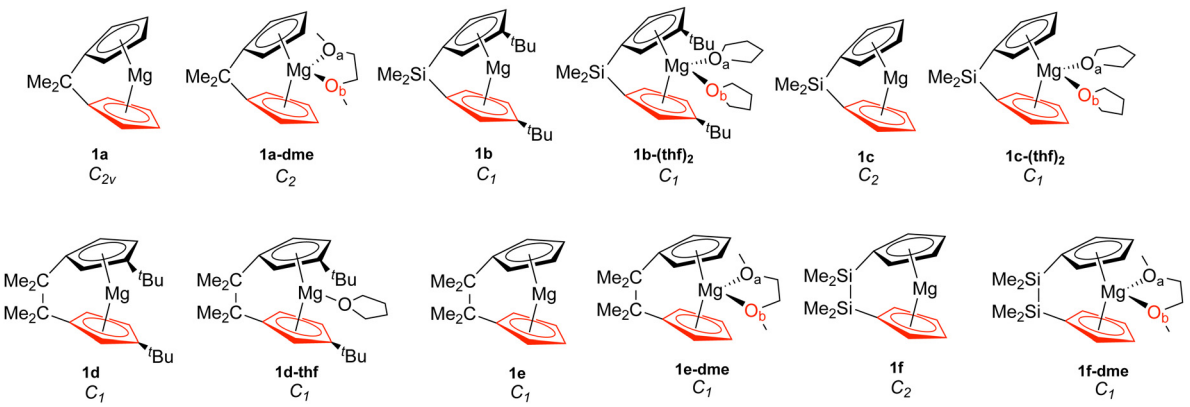

Fig. 1 Magnesocenophanes (**1**). The bottom Cp ring is highlighted in red, while O_a is in black and O_b is in red.

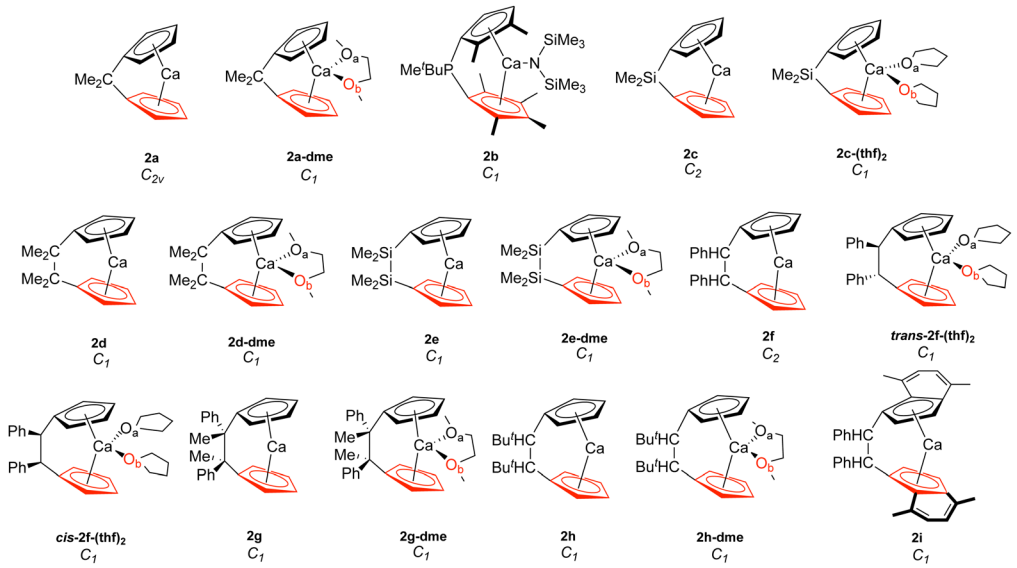

Fig. 2 Calcocenophanes (**2**). The bottom Cp ring is highlighted in red, while O_a is in black and O_b is in red.

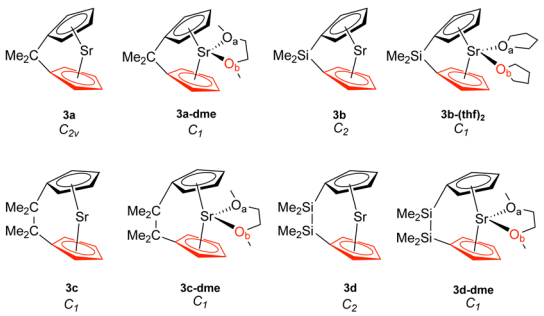

Fig. 3 Strontiocenophanes (**3**). The bottom Cp ring is highlighted in red, while O_a is in black and O_b is in red.

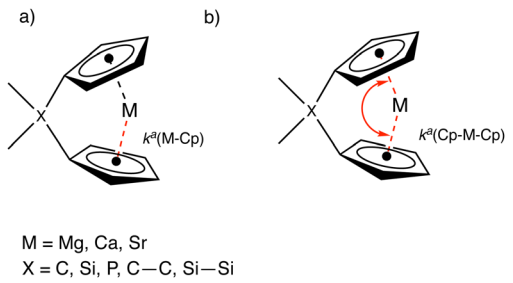

Fig. 4 Special force constants used in this work. (a) Local force constant between the metal (M) and geometric centerpoint of the Cp ring k^a(M–Cp). (b) Local force constant between the Cp–M–Cp angle k^a(Cp–M–Cp).

BSOs and force constants are utilized to obtain the parameters for A and B, with the constraint that a zero value for the force constant k^a equals a zero BSO value. To characterize Mg–O interactions, the reference molecules used were MgH_2 for the single bond character (BSO = 1) and Mg=O for the double bond (BSO = 2) character,[44] with A and B values being 0.7338 and 0.7546, respectively. To characterize Ca–O interactions, the reference molecules used were CaH_2 for the single bond character and Ca=O for the double bond character,[45] with A and B values being 1.0391 and 0.4784, respectively. To characterize Sr–O interactions, the reference molecules used were SrH_2 for the single bond character and Sr=O for the double bond character, with A and B values being 1.1409 and 0.4418, respectively. Generally, a discussion in terms of BSO values is chemically more intuitive than the comparison of force constant values.

LMA was complemented with the topological analysis of the electron density using Bader's quantum theory of atoms in molecule (QTAIM).[46–48] The covalent character of the M–O (where M = Mg, Ca, and Sr) interactions was assessed *via* the Cremer–Kraka criterion,[49,50] which is based on the value of the energy density $H(r)$ taken at the bond critical point $\boldsymbol{r}_b$ on the electron density bond path between the two atoms involved in the chemical bond or weak chemical interaction.[46–48] A negative value of $H(r)$ indicates the covalent character of the bond/interaction, whereas a positive $H(r)$ value signifies a predominantly electrostatic interaction between the two atoms under consideration. To gain further insight into the electronic structure, specifically with the M–Cp interaction and the effects of the bridging motifs, Laplacian maps were created within the Cp–M–Cp plane. The Laplacian of the electronic density $\nabla^2(\rho(r))$ reveals local regions of charge depletion (positive $\nabla^2(\rho(r))$ values) and charge concentration (negative $\nabla^2(\rho(r))$ values).[51,52]

Starting geometries of the solvent-bound (THF or DME) *ansa*-metallocenes were obtained from previous experimental crystal structures.[7,15–23] For the structures where no solvent was attached to the group 2 metal, the crystal structure was edited to remove the solvent(s) attached. The geometries and frequencies were calculated for 37 structures ranging from

[1]magnesocenophanes, [2]magnesocenophanes, [1]calcocenophanes, [2]calcocenophanes, [1] strontiocenophane, and [2]strontiocenophane, as well as four metallocene structures (ESI,† Fig. S1)[30] for comparison (**A**–**D**) using the B3LYP functional[53,54] with Grimme's D3 dispersion correction zero damping[55] (shortened to B3LYP-D3) in combination with the def2-TZVP basis set[56] in the gas phase. All DFT calculations were carried out with the Gaussian 16 program[57] using an ultrafine grid and a tight convergence criterion for the self-consistent field step. Frequency calculations of all complexes were completed without imaginary normal mode frequencies and followed by subsequent local mode analysis of M–Cp, and M–O bonds, and Cp–M–Cp angles utilizing the LModeA program.[58] Natural population charges were calculated utilizing the natural bond orbital (NBO) analysis implemented in the NBO7 program.[59] QTAIM calculations were done with the AIMALL package.[60]

Results and discussion

Table 1 displays the distance d (Å) between the metal and the Cp ring(s) with the corresponding local force constant k^a(M–Cp) (mdyn/Å), the angle A (°) for Cp–M–Cp with the corresponding local force constant k^a(Cp–M–Cp) (mdynÅ/Rad^2), and the natural charge (e) of the metal. For the structures that have distances and local force constants of M–Cp that differ, the top row corresponds to the top Cp ring while the bottom row corresponds to the bottom Cp ring. Fig. 5(a) shows the relationship between the M–Cp bond length and the local force constant and Fig. 5(b) shows the relationship between the Cp–M–Cp bond angle and k^a(M–Cp). In Fig. 6(a)–(c), the correlation between the bond length and the local mode force constant is depicted for the Mg–Cp, Ca–Cp, and Sr–Cp bonds, respectively. Table 2 shows BSO n values of M–O_a and M–O_b, distances of M–O_a and M–O_b (Å), local mode force constants k^a(M–O_a) and k^a(M–O_b), and the angle A (°) between O_a–M–O_b and the corresponding local force constant k^a(O_a–M–O_b). Fig. 7(a) and (b) shows BSO n values as a function of the local mode force constants for the Mg–O and Ca–O bonds formed between the metal and THF or DME oxygen(s), respectively. Fig. 7(c) displays the relationship between the energy density $H(r)$ (Hartree/Å^3) and the local force constant k^a(M–O). Fig. 8(a) shows the relationship between the Cp–M–Cp bond angles and the corresponding local force constant k^a(Cp–M–Cp), while Fig. 8(b) displays the relationship between the charge on M and the local force constant k^a(Cp–M–Cp). Fig. 9 displays the Laplacian of electronic density $\nabla^2(\rho(r))$ for some of the complexes investigated.

M–Cp bond length, Cp–M–Cp bond angle and local mode M–Cp force constant

To investigate the relationship between the nature of group 2 metals and the M–Cp bond in *ansa*-metallocene structures, the trend between the bond length and the local force constant of M–Cp for group 2 metals (Mg, Ca, and Sr) is plotted in Fig. 5(a). There is an obvious trend between the metal that characterizes the *ansa*-metallocenes and the distance/local force strength encountered. This trend starts with magnesocenophanes having the metal and Cp rings closer together (with a range from

Table 1 Calculated M–Cp distances (M = Mg, Ca, or Sr) d (Å), local mode force constants k^a (M–Cp) (mdyn/Å), Cp–M–Cp angles A (°), and corresponding local mode force constants k^a(Cp–M–Cp) (mdynÅ/Rad^2), as well as NBO charges for the metal. For structures whose distances and local force constants of M–Cp differ, the top row corresponds to the top Cp ring, while the bottom row corresponds to the bottom Cp ring (for more information, see the text) at the B3LYP-D3/def2-TZVP level of theory

Structure	d	k^a (M–Cp)	A	k^a (Cp–M–Cp)	e
1a	2.003	1.551	126.6	1.043	1.776
1a-dme	2.156	0.321	125.3	1.021	1.811
1b	2.000	1.578	139.4	0.805	1.816
1b-(thf)$_2$	2.122	0.933	127.2	0.577	1.827
	2.188	0.370			
1c	2.004	1.539	138.9	0.806	1.794
1c-(thf)$_2$	2.120	0.927	128.3	0.644	1.820
	2.165	0.308			
1d	1.975	1.735	140.2	0.737	1.825
	1.976	1.749			
1d-thf	2.092	1.052	135.5	0.662	1.841
	2.108	1.036			
1e	1.981	1.693	139.6	0.737	1.800
1e-dme	2.156	0.629	133.4	0.568	1.816
1f	1.992	1.673	160.2	0.510	1.817
1f-dme	2.108	1.046	148.2	0.529	1.808
	2.241	0.370			
2a	2.310	1.450	114.6	2.092	1.726
2a-dme	2.361	1.157	112.8	1.992	1.719
	2.365	1.144			
2b	2.500	0.715	117.2	1.318	1.776
	2.508	0.718			
2c	2.326	1.394	125.8	1.596	1.743
2c-(thf)$_2$	2.411	1.018	122.7	1.568	1.745
	2.400	1.053			
2d	2.307	1.576	125.4	1.389	1.751
2d-dme	2.360	1.302	122.0	1.319	1.734
2e	2.335	1.440	143.6	0.635	1.771
2e-dme	2.401	1.132	138.0	0.820	1.746
	2.400	1.128			
2f	2.316	1.536	124.8	1.415	1.748
***trans*-2f-thf**	2.392	1.196	120.9	1.428	1.749
	2.401	1.136			
***cis*-2f-thf**	2.387	1.191	122.0	1.344	1.750
	2.383	1.238			
2g	2.306	1.578	125.5	1.305	1.753
	2.310	1.570			
2g-dme	2.356	1.314	122.6	1.223	1.736
	2.367	1.296			
2h	2.296	1.585	124.5	1.36	1.751
	2.310	1.539			
2h-dme	2.363	1.255	121.9	1.319	1.735
	2.346	1.326			
2i	2.319	1.431	123.3	1.075	1.754
	2.312	1.425			
3a	2.485	1.310	108.1	2.441	1.757
3a-dme	2.535	1.094	106.4	2.292	1.760
	2.536	1.046			
3b	2.507	1.237	118.8	1.877	1.772
3b-(thf)$_2$	2.579	0.964	116.3	1.724	1.778
	2.571	0.928			
3c	2.489	1.412	118.5	1.560	1.781
3c-dme	2.534	1.199	116.9	1.465	1.772
	2.530	1.222			
3d	2.523	1.271	135.8	0.774	1.801
3d-dme	2.573	1.054	133.5	0.775	1.783
	2.570	1.085			

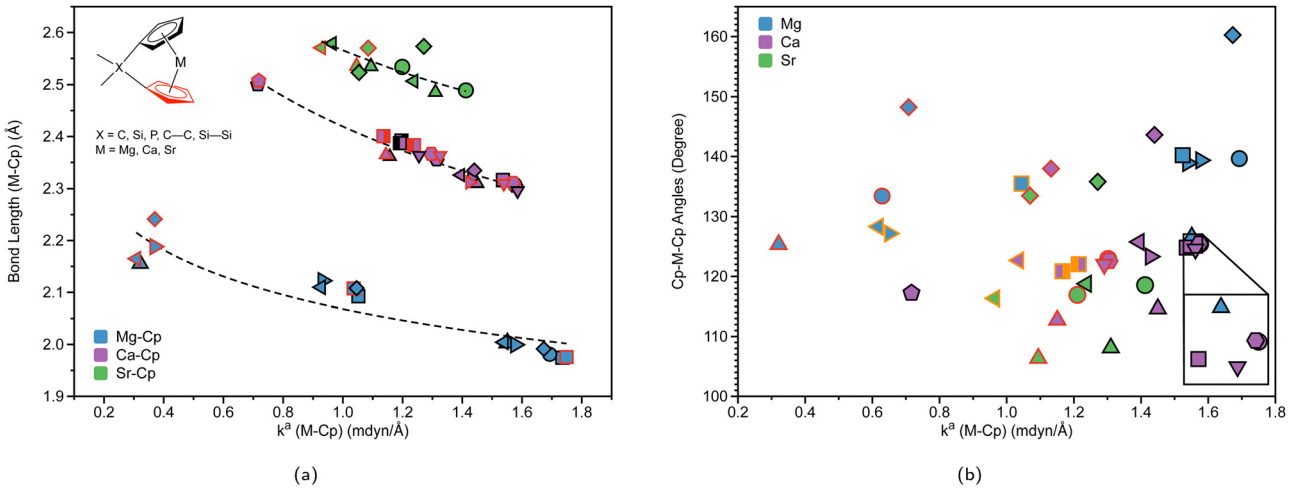

Fig. 5 (a) M–Cp bond length (Å) (where M = Mg (blue), Ca (purple), or Sr (green)) *vs.* local force constant k^a(M–Cp) (mdyn/Å). The black outline represents the top portion of the ring and the red outline represents the bottom portion of the Cp ring. The dashed lines for each group are displayed for clarity. (b) Cp–M–Cp angles (degree) *vs.* local force constant k^a(M–Cp) (mdyn/Å). For clarity, the average of the k^a(M–Cp) top and bottom rings is displayed. The black outline represents non-solvated structures, the red outline represents DME-solvated structures, and the orange outline represents THF-solvated structures. For more information regarding the symbol labels, the reader is referred to Fig. 6(a) and (b), where the same symbols are utilized at the B3LYP-D3/def2-TZVP level of theory.

1.981 to 2.241 Å), and is confirmed by the local force constants, with longer bonds having a lower local force constant and shorter bonds having a higher local force constant. As we go down the periodic table and increase the size of the atom from Mg to Ca, the length of M–Cp increases (with a range from 2.296 to 2.508 Å), which is again confirmed by the local force constants (*i.e.* longer bonds having a lower force constant). Increasing the size from Ca to Sr, the length of M–Cp increases (with a range from 2.485 to 2.579 Å). It is interesting to note that as the bond length of the M–Cp bond increases as we go down the periodic table, the local force constant does not dramatically change as one might expect. For example, **1e** has a bond length of 1.981 Å and a local force constant of 1.673 mdyn/Å, whereas **2d**, which has the same [2]carbon bridging motif as **1e**, has a bond length of 2.307 Å and a local force constant of 1.576 mdyn/Å. Although there is a slight lengthening of the M–Cp bond from Mg to Ca, the local force constant only slightly decreases in strength. If we go down the periodic table again to Sr (**3c**), the bond length of the Sr–Cp bond is 2.489 Å, while the local force constant is 1.412 Å, further decreasing slightly in the bond strength as the bond length increases. This is indicative that the strength of the M–Cp bond(s) is not only dependent on the nature of the metal but also dependent on the stability that the bridging motifs bring.

For further insight, the relationship between the Cp–M–Cp bond angle and k^a(M–Cp) was analyzed, as shown in Fig. 5(b). It appears that there is no general or periodic trend observed concerning the Cp–M–Cp angle and the M–Cp force constant. There is a general effect on the nature of the metal; as one goes from Mg to Sr, the Cp–M–Cp angle decreases, as shown for [2]sila-bridging motifs (139.6° for **1e**, 125.4° for **2d**, and 118.5° for **3c**) and we also see that the M–Cp bond strength effectively decreases (1.981 mdyn/Å, 1.576 mdyn/Å, and 1.412 mdyn/Å, respectively). When looking at qualitative assessments such as an orbital overlap, one can propose that the change of the angle where the metal effectively slips out of the ring changes the overlap between the Cp rings and the metal. With our local force constants as a complementary tool, the changes of the M–Cp strength coupled with the Cp–M–Cp angles can be tracked quantitatively. It is observed that there is a solvation effect, with the binding of THF or DME decreasing the angle and subsequently the bond strength of M–Cp. For magnesocenophanes, the bridging motifs going from [1]sila to [2]carba does not drastically change the angle. For example, **1b** and **1c** (which are [1]sila magnesocenophanes) have similar angles and k^a(M–Cp) bond strengths (139.4°, 1.578 mdyn Å^{-1} and 138.9°, 1.539 mdyn Å^{-1}, respectively), while **1d** and **1e** (which are [2]carba-magnesocenophanes) have similar angles and k^a(Mg-Cp) average to their [1]sila-counterpart (140.2°, 1.524 mdyn/Å and 139.6°, 1.693 mdyn/Å, respectively). Going from a [2]carba-bridging motif to a [2]sila-motif increases the angle by about 20° for magnesocenophanes. For calcocenophanes, the bridging motifs going from [1]carba to [1]sila (**2a** to **2c**) only changes the angle 10°, with a minimal change in the k^a(Ca–Cp) force constant (1.450 mdyn/Å for **2a** and 1.394 mdyn/Å for **2c**). Going from a [2]carba-motif to a [2]sila-motif (**2d** to **2e**), we see a similar increase in the angle as shown for the one-atom-bridged motif counterpart. The bond strength between the Ca–Cp going from [2]carba to [2]sila slightly decreases (1.576 mdyn/Å for **2d** and 1.440 mdyn/Å for **2e**). For calcocenophanes, since these structures are primarily experimentally characterized with [2]carba-bridging motifs, the bond angles, as well as the k^a(M–Cp) do not differ much for the non-solvated structures (with the only exception being **2i**, most likely due to the addition of the ring, and **2e**, most likely due to the Si atom).

To gain insight into the effects that solvated structures have in characterizing magnesocenophanes, calcocenophanes, and strontiocenophanes, individual M–Cp bond lengths *versus* local

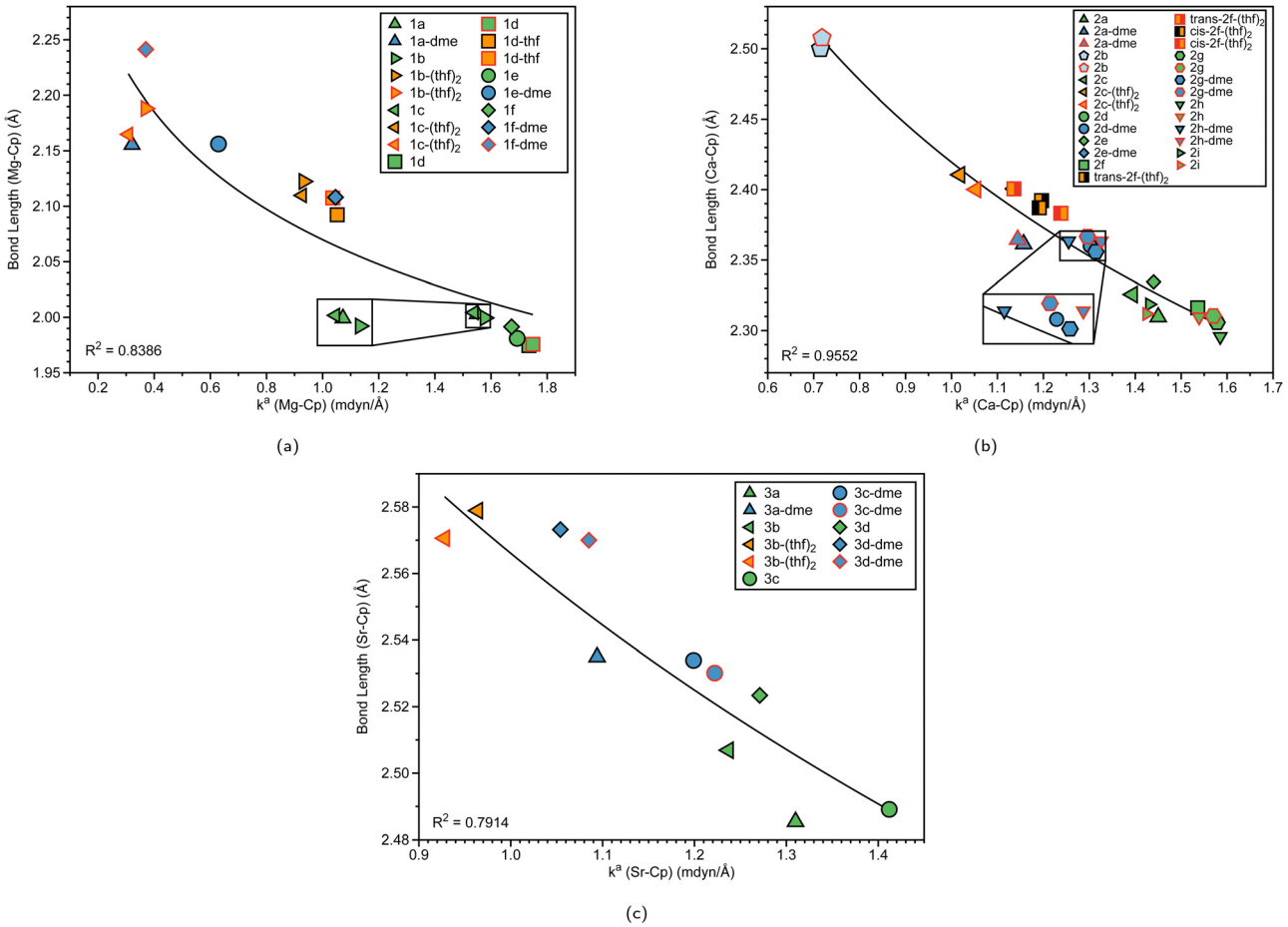

Fig. 6 (a) Mg–Cp bond length (Å) *vs.* local force constant k^a (Mg–Cp) (mdyn/Å). (b) Ca–Cp bond length (Å) *vs.* local force constant k^a (Ca–Cp) (mdyn/Å). (c) Sr–Cp bond length (Å) *vs.* local force constant k^a(Sr–Cp) (mdyn/Å). The black outline represents the top portion of the ring and the red outline represents the bottom portion of the Cp ring at the B3LYP-D3/def2-TZVP level of theory.

force constants are displayed in Fig. 6(a) for magnesocenophanes, Fig. 6(b) for calcocenophanes, and Fig. 6(c) for strontiocenophanes. As shown in more detail in Fig. 6(a), the solvent(s) that are typically present in characterizing these magnesium-containing metallocenophane structures through X-ray crystallography (whether THF or DME) drastically affect the strength of the Mg–Cp bond by decreasing the local force constant and increasing the bond length of the Mg–Cp bond(s) compared to its non-solvated counterpart. For example, in **1a,** the Mg–Cp distance is 2.003 Å with a force constant of 1.551 mdyn/Å, whereas in **1a-dme,** it is 2.156 Å with a force constant of 0.321 mdyn/Å. It is also evident that the effect of binding to THF or DME in magnesocalcenophanes breaks the apparent Mg–Cp symmetry of the structure, as shown in Fig. 6(a), where green colored points indicate non-solvated structures, orange indicates the THF solvent that is bound to the structure(s), and blue indicates the DME solvent that is bound to the structure(s). There is also clustering of the top and bottom Mg–Cp rings for solvent-bound magnesocenophanes (Fig. 6(a), black (top ring) and red (bottom ring) outline for **1b-(thf)$_2$**, **1c-(thf)$_2$**, **1d-thf**, and **1f-dme**). It appears that most solvated magnesocenophane structures (except for **1a-dme** and **1e-dme**) have the top Cp ring closer to the Mg metal (an average of 2.108 Å) and the stronger local force constant (an average of 0.989 mdyn/Å) than the bottom Cp ring (which has average values of 2.175 Å and 0.521 mdyn/Å). It is important to note the significance of the decrease in the local force constant and an increase in the bond length for the solvent-coordinated Mg–Cp rings since these compounds are usually characterized as intermediates in catalysis to prepare transition metal metallocenophanes.[24] Utilizing the LMA, it is observed that the solvent-coordinated magnesium-containing *ansa*-metallocenophanes have a weaker local force constant than its non-solvated counterpart, allowing for Mg to be replaced with a transition metal with more ease. This makes the LMA a powerful tool to capture the strong influence that solvent coordination can have on the overall geometry and ability of magnesocenophanes to be used in transmetalation reactions.

Similar to the magnesocenophane trend that was seen for solvent-containing compounds, solvent-bound calcocenophanes show a slight decrease in the local force constant k^a(Ca–Cp) and bond length as shown in Fig. 6(b). There is a trend between the solvated structures and the non-solvated structures, with the THF solvated structures (**2c-(thf)$_2$**, ***trans*-2f-(thf)$_2$**

Table 2 Calculated bond strength order (BSO n) for M–O_a (M = Mg, Ca, or Sr), BSO for M–O_b, M–O_a distances d (Å), M–O_b distances d (Å), local mode force constants k^a (M–O_a) (mdyn/Å), k^a (M–O_b) (mdyn/Å), O_a–M–O_b angles A (°), and corresponding local mode force constant k^a(O_a–M–O_b) at the B3LYP-D3/def2-TZVP level of theory

Structure	BSO n (M–O_a)	BSO n (M–O_b)	d (M–O_a)	d (M–O_b)	k^a (M–O_a)	k^a (M–O_b)	A	k^a (O_a–M–O_b)
1a-dme	0.456	0.456	2.126	2.126	0.532	0.532	76.3	1.486
1b-(thf)$_2$	0.515	0.575	2.110	2.083	0.626	0.723	91.8	0.500
1c-(thf)$_2$	0.593	0.617	2.072	2.068	0.754	0.795	88.0	0.531
1d-thf	0.520		2.096		0.634			
1e-dme	0.320	0.320	2.186	2.187	0.333	0.333	73.9	1.350
1f-dme	0.396	0.490	2.170	2.107	0.441	0.586	75.1	1.455
2a-dme	0.681	0.681	2.470	2.472	0.414	0.414	68.3	1.341
2c-(thf)$_2$	0.798	0.717	2.401	2.442	0.576	0.461	79.3	0.369
2d-dme	0.687	0.687	2.479	2.479	0.421	0.421	67.9	1.418
2e-dme	0.671	0.671	2.481	2.484	0.401	0.401	67.7	1.449
***trans*-2f-(thf)$_2$**	0.699	0.774	2.453	2.420	0.436	0.541	79.4	0.326
***cis*-2f-(thf)$_2$**	0.789	0.723	2.405	2.434	0.563	0.468	79.6	0.347
2g-dme	0.691	0.685	2.476	2.478	0.426	0.418	67.9	1.431
2h-dme	0.678	0.684	2.481	2.479	0.409	0.417	67.9	1.408
3a-dme	0.734	0.658	2.646	2.711	0.369	0.288	63.2	1.422
3b-(thf)$_2$	0.786	0.718	2.598	2.641	0.430	0.351	77.0	0.301
3c-dme	0.694	0.693	2.672	2.675	0.325	0.324	63.6	1.424
3d-dme	0.715	0.719	2.658	2.657	0.347	0.352	64.0	1.463

and ***cis*-2f-(thf)$_2$**) grouped (an average M–Cp bond length of 2.396 Å and a force constant of 1.139 mdyn/Å), and the DME solvated structures (**2e-dme**, **2g-dme** and **2h-dme**) grouped (an average bond length of 2.372 Å and a force constant of 1.242 mdyn/Å). The only outlier that is not grouped in its appropriate solvation group is **2d-dme**, the [2]carba-calcocenophane motif, which has a bond length of 2.360 Å and a strength of 1.302 mdyn/Å, which is higher than the DME Ca–Cp average. It is important to note that structure **2b** (the light blue pentagon in Fig. 6(b)) does have an amide group attached to the calcium, has phosphorus as the bridging atom, and instead of the typical Cp ring that is utilized for *ansa*-metallocenes, is pentamethyl cyclopentadiene (Cp*). Unlike the magnesocenophane non-solvated structures, the calcocenophane structures that are not solvated have slightly different Ca–Cp bond lengths/force constants, displaying a lack of symmetry in these structures. This could be due to its primary bridging motif, which, unlike magnesocenophanes, comprises mostly [2]carba-calcocenophanes, with different branching points from the carbon, such as the addition of phenyl groups (**2f**, ***trans*-2f-(thf)$_2$**, ***cis*-2f-(thf)$_2$**, and **2i**), methyl and phenyl groups (**2g**) and *tert*-butyl groups (**2h** and **2h-dme**). Similar to magnesocenophanes, the synthetic uses of these calcocenophanes are typical for transmetalation reactions and are typically seen as an impurity when carrying out reductive elimination reactions.[20]

Although we see a similar trend between the non-solvated and the solvated strontiocenophanes, it is not as separated as seen for the magnesocenophane and calcocenophanes, as shown in Fig. 6(c). The strongest and shortest non-solvated Sr–Cp bond is the [2]carba-bridged motif **3c** (2.489 Å and 1.412 mdyn/Å), with the weakest and longest non-solvated Sr–Cp bond is the [2]sila-bridged motif **3d** (2.523 Å and 1.271 mdyn/Å). Solvation further decreases the bond strength, however, not as much, with the strongest solvated Sr–Cp bond coming from **3c-dme** (an average of 1.211 mdyn/Å between the two rings). Overall, the weakest Sr–Cp bond comes from the [1]sila-motif with solvation (**3c-(thf)2**), an average of 0.946 mdyn/Å between the two rings, with a bond length of 2.575 Å. It appears that the one-atom-bridged silicon, coupled with solvation, decreases the strength for the M–Cp bond, which was also seen for magnesocenophanes (**1e-dme**) and calcocenophanes (when disregarding **2b**, **2c-(thf)$_2$**).

Mg–O and Ca–O interactions with solvent molecules

To further investigate the effect of the solvent(s) (THF or DME) binding to group 2 *ansa*-metallocenes, we have plotted the BSO of the Mg–O and Ca–O interactions with respect to the local force constant (mdyn/Å) in Fig. 7(a) and (b), respectively. Table 2 also displays information on the bond distances, angles, and force constants of the M–O_a and M–O_b bonds, including Sr–O. If a structure is bound to two oxygens that have different corresponding bond strengths, the oxygens are labeled in Fig. 1–3, where O_a is indicated as a black outline, and O_b is indicated as a red outline. For the solvent-bound magnesocenophane systems in Fig. 7(a), most of the systems (except for **1d-thf**) have two oxygens bound to Mg. For the other DME solvated structure, **1f-dme**, Mg–O_a has a BSO of 0.440 and a local force constant of 0.396 mdyn/Å, whereas for Mg–O_b, the local force constant and BSO increase (0.586 mdyn/Å and 0.490 respectively). The same trends are seen for THF-solvated structures, where the Mg–O_a bond has a smaller BSO and local a force constant, indicating that it is weaker than its Mg–O_b counterpart. It is also interesting to note that the DME-bound structures have weaker Mg–O bonds and the THF-solvated systems have stronger Mg–O bonds. A previous experimental investigation for dehydrocoupling reactions in [1]carba magnesocenophanes showed that the catalytic activity was lower in THF complexes than that in DME complexes, which our theoretical insight supports.[15] For solvated calcocenophanes, as shown in Fig. 7(b), similar trends are seen as previously described in solvated magnesocenophane systems, where Ca–O_a bonds are weaker than the Ca–O_b bonds. However, for

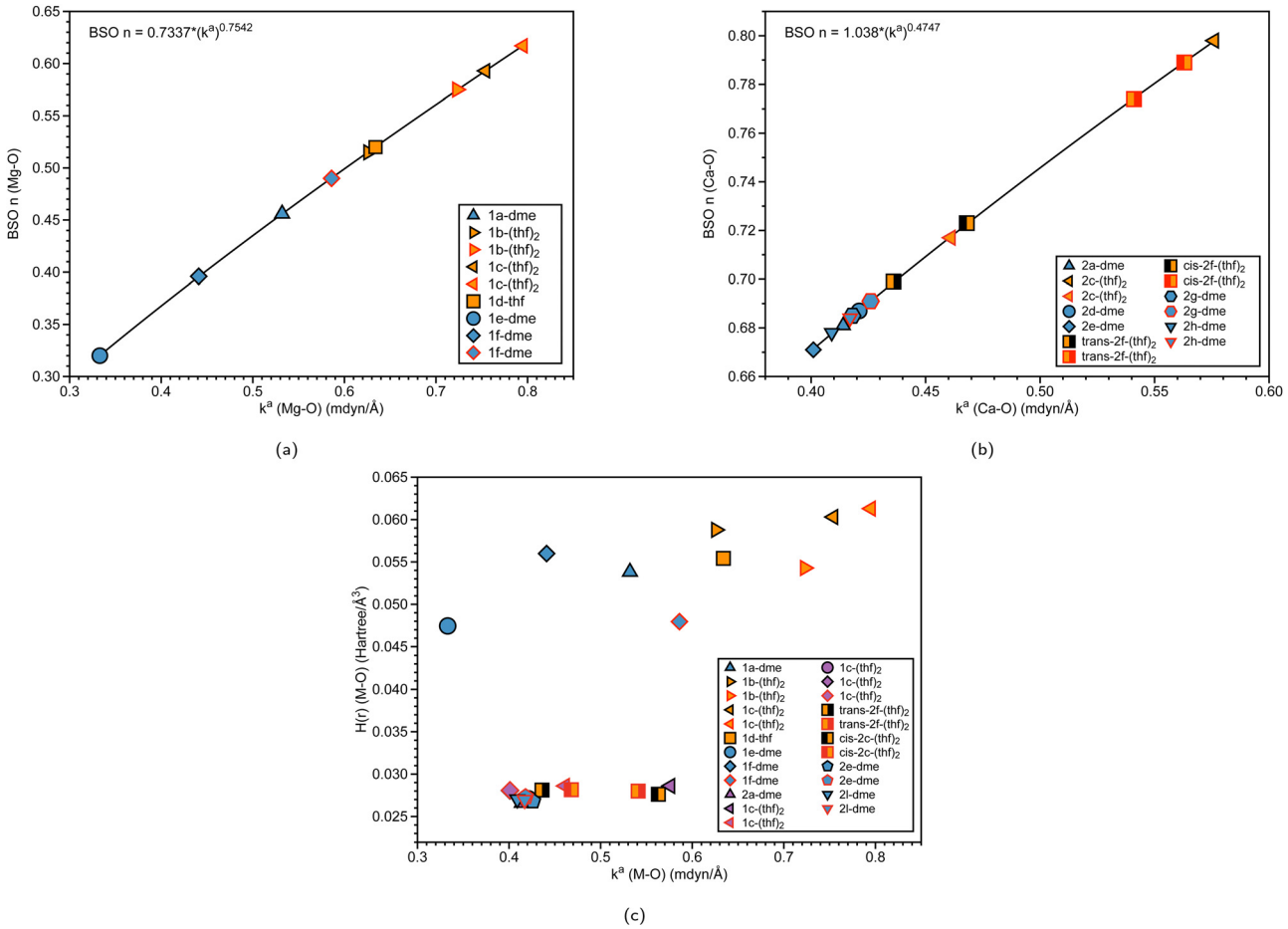

Fig. 7 (a) BSO *n* (Mg–O) *vs.* local force constant k^a(Mg–O) (mdyn/Å). (b) BSO *n* (Ca–O) *vs.* local force constant k^a(Ca–O) (mdyn/Å). The black outline represents O_a, while the red outline represents O_b (see Fig. 1 and Fig. 2). (c) Energy density *H*(*r*) (Hartree/Å^3) *vs.* local force constant k^a(M–O) (where M = Mg, Ca). The black outline represents O_a, while the red outline represents O_b at the B3LYP-D3/def2-TZVP level of theory.

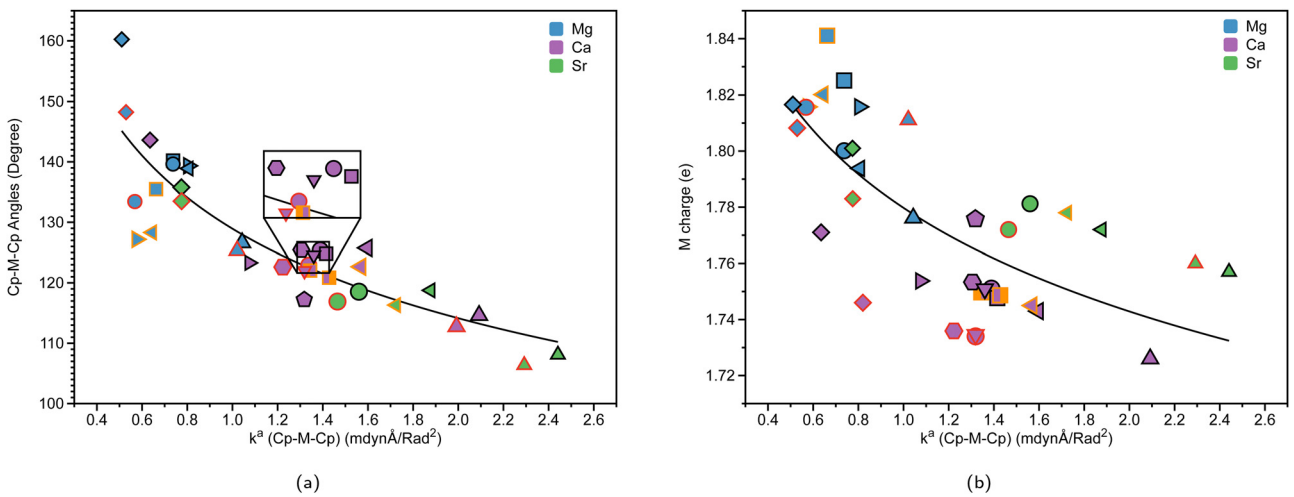

Fig. 8 (a) Cp–M–Cp angles (degree), (where M = Mg (blue), Ca (purple), or Sr (green)) *vs.* local force constant k^a(Cp–M–Cp) (mdynÅ/Rad^2). (b) NBO charge on M (*e*) *vs.* k^a(Cp–M–Cp) (mdynÅ/Rad^2). The black outline represents non-solvated structures; the red outline represents DME-solvated structures, and the orange outline represents THF-solvated structures at the B3LYP-D3/def2-TZVP level of theory.

2g-dme and **2h-dme**, going from Ca–O_a to Ca–O_b slightly increases in the bond strength (0.008 mdyn/Å increase) and for ***trans*-2f-(thf)$_2$** and ***cis*-2f-(thf)$_2$**, it increases a bit more (0.105 mdyn/Å and 0.095 mdyn/Å increase, respectively). While

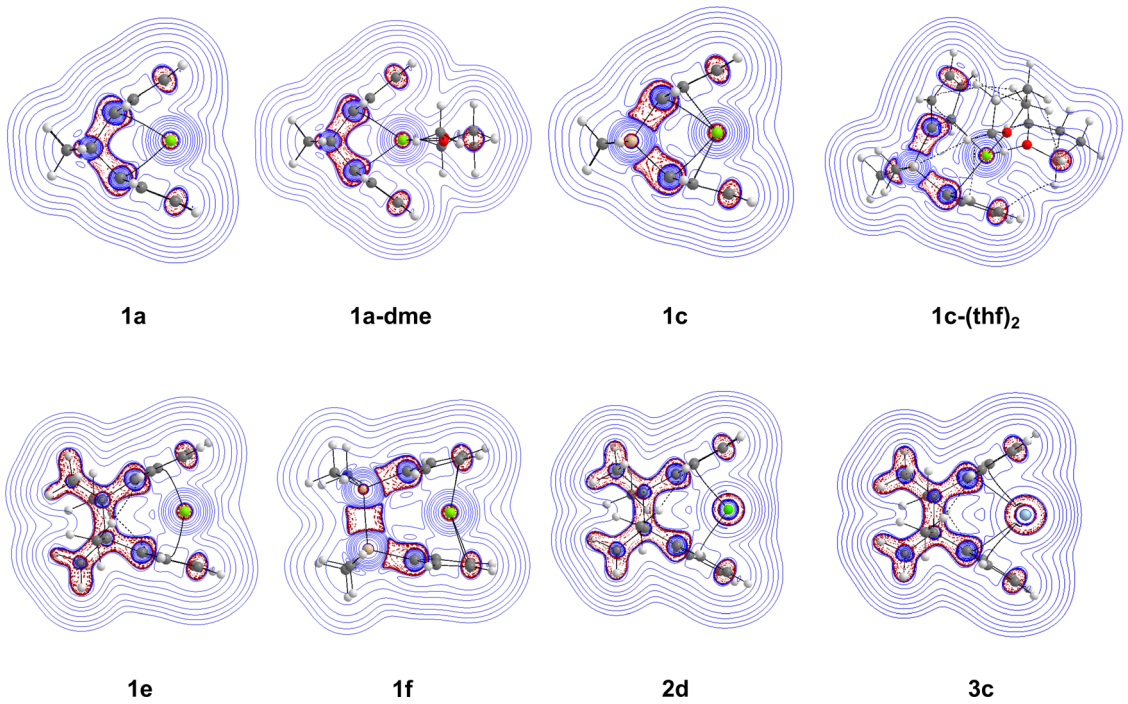

Fig. 9 Contour plots displaying the Laplacian of the electron density within the Cp–M–Cp plane for **1a**, **1a-dme**, **1c**, **1c-(thf)$_2$**, **1e**, **1f**, **2d**, and **3c**. The blue solid lines account for positive $\nabla^2(\rho(r))$ values (depletion of the charge)), while the red dashed lines represent negative $\nabla^2(\rho(r))$ values (concentration of the charge) at the B3LYP-D3/def2-TZVP level of theory.

there are not many solvated molecules for the strontiocenophanes, looking at Table 2 shows that the same trend still applies, with only the M–O_b bond from **3d-dme** having a similar bond strength to that from **3b-(thf)$_2$**. We also see for THF structures, the O_a–M–O_b bond is greater than DME structures, which is also indicated by weaker local force constants (which indicates a less stiff bond, whereas for the DME structures, the angles are much more acute, followed by a greater local force constant for the angle). Overall, as reflected by the BSO values, the Mg–O and Ca–O interactions are weaker than a single bond.

We also investigated the covalent character of the M–O bond *via* the inspection of the electron density $H(r)$. Fig. 7(c) shows the relationship between $H(r)$ (M–O) and the local force constant k^a(M–O), with the black outline representing O_a and the red outline representing O_b. It is apparent that the magnesocenophane metal–oxygen bonds have more electrostatic characters than the calcocenophane counterparts. For magnesocenophanes, when going from Mg–O_b to Mg–O_a, the electrostatic character typically increases (except for **1c-(thf)$_2$**, where it decreases) as the local force constant decreases. Overall, for calcocenophanes, $H(r)$ values are similar to those of DME and THF-bound oxygen, a trend which is also seen in Fig. 7(b).

Cp–M–Cp angle bending and stiffness

To explore the correlation between Cp–M–Cp angles and the relative stiffness of *ansa*-metallocenes, the LMA was conducted on the systems investigated. Fig. 8(a) presents the relationship between the bond angles of Cp–M–Cp for the group 2 metals (Mg (blue), Ca (purple), and Sr (green)) and its local force constant counterpart. Fig. 8(b) shows the relationship between the charge of the group 2 metal (e) and the local force constant k^a(Cp–M–Cp) indicating the stiffness of the angle indicated. The black outline in Fig. 8(a) and (b) refers to non-solvated structures, whereas the red outline represents DME-solvated structures, and the orange outline represents THF-solvated structures. The Cp–Mg–Cp angles in magnesocenophanes range from 125.4° to 160.2°. For magnesium-containing *ansa*-metallocenes, the non-solvated structures (black outline) show a trend that as the angle between the Cp–Mg–Cp bond decreases, the force constant increases. The effect of the [1]carba/[1]sila magnesocenophanes and [2]carba/[2]sila magnesocenophanes bridging motifs is evident in these trends. For example, going from [1]carba magnesocenophane **1a** to [1]sila magnesocenophane **1c** increases the bond angle from 126.6° to 138.9°, which is reflected by the decrease in the local force constant (1.043 mdynÅ/Rad^2 to 0.806 mdynÅ/rad^2). This trend is also seen going from [2]carba magnesocenophane **1e** to [2]sila magnesocenophane **1f**. What the local force constant from LMA captures is the ability to measure stiffness and compare these bond angles amongst each other, as we see here with the stiffness decrease as we change the bridging motif atom from carbon to silicon. Therefore, one could propose that if one wants a very stiff magnesocenophane structure, utilizing a [1]carba-bridging motif will yield beneficial results, whereas if one wants a more relaxed Cp–Mg–Cp angle, the [2]sila-bridged magnesocenophane would be the most optimal option. The effect that solvation has on the stiffness of the Cp–Mg–Cp angle

is evident as well, showing that the local force constant and angle decrease for solvent-coordinated structures. For example, **1d** (blue square, black outline) has an angle of 140.2° and a local force constant of 0.737 mdynÅ/Rad^2, whereas **1d-thf** (blue square, orange outline) has an angle of 135.5° and a local force constant of 0.662 mdynÅ/rad^2.

For calcocenophanes, the angles range from 114.6° to 143.6°. We see a similar trend that as the angle increases, the force constant decreases for non-solvated structures (black outline). Going from [1]carba calcocenophane **2a** to [1]sila calcocenophane **2c** increases the bond angle from 114.6° to 125.8°, with a decrease in the local force constant (2.092 mdynÅ/Rad^2 to 1.596 mdynÅ/rad^2). When one goes from a [2]carba calcocenophane **2d** to a [2]sila calcocenophane **2e**, the angle also increases as well from 125.4° to 143.6° (with a decrease in the local force constant of the Cp–M–Cp angle). It is important to note that most structures have different substituents on the Cp ring and bridging motifs among the [2]carba-calcocenophanes, particularly **2f–2i**. The same trend where the angle increases going from a one-atom to two-atom bridged motif that was seen for [2]carba/sila magnesocenophanes is also seen for [2]carba/sila calcocenophanes. Considering solvation effects, LMA does capture the differences in the bond angle stiffness as one goes from non-solvated structures to solvated structures. The same trend seen in magnesocenophanes with regard to solvated structures is seen with calcocenophanes. For example, going from **2g** (purple pentagon, black outline), which has an angle of 122.6° and a local force constant of 1.360 mdyn Å rad^{-2}, to DME-solvated **2g-dme** (purple pentagon, red outline) decreases the angle and force constant (121.9° and 1.319 mdynÅ/Rad^2, respectively). This angle and local force constant decrease from non-solvated to solvated structures is seen in both magnesocenophanes and calcocenophanes alike. It is also interesting to note that the [2]carba calcocenophanes that have a phenyl ring attached to the carbons instead of a methyl group (**2f**, ***trans*-2f-(thf)$_2$**, ***cis*-2f-(thf)$_2$**, **2g**, **2g-dme**, **2h**, **2h-dme**, and **2i**) all have similar bond angles 120°–124°, most likely due to the rigidity and the steric effects of the motifs.

For strontiocenophanes, the same trend is observed, with the range of Cp–M–Cp angles being from 106.4° to 135.8°. Going from a [1]carba strontiocenophane to a [1]sila strontiocenophane increases the angle from 108.1° to 118.8°, which is reflected with the decrease in the corresponding local force constant (2.441 mdynÅ/Rad^2 to 1.877 mdynÅ/Rad^2). Overall, the stiffness of the Cp–M–Cp increases as you go down the group 2 metals (from Mg (blue), Ca (purple) to Sr (green)), as exhibited by the local force constant for Cp–M–Cp increasing with the bond angle decreasing as well. Fig. 8(a) displays that there is no periodic trend as observed previously; however, there are similar groupings based on the bridging motif (for example, the [2]sila calcocenophane/[2]sila strontiocenophane indicated by diamond purple and diamond green, respectively). Previous computational investigation into group 2 metallocenes without the *ansa*-bridging motif displays similar trends as one goes down the group 2 periodic table, the angle between the Cp–M–Cp decreases, losing its linear structure (~180°) and becoming more bent.[61]

As shown in Fig. 8(b), which shows the charge of the metal corresponding with the stiffness of the Cp–M–Cp bond (k^a(Cp–M–Cp)), there appears to be not much of a periodic trend between the angle of Cp–M–Cp and stiffness (k^a(Cp–M–Cp)), indicating that the bridging motifs, as well as the solvation of THF or DME can affect the stiffness of the Cp–M–Cp angle, and the charge of the atom. Another interesting thing to note is that for magnesocenophanes, the addition of solvation appears to slightly increase the charge of the metal (the red/orange outline is a greater charge in Fig. 8(b) than the black outline). For calcocenophanes, it appears that this is not the trend observed, with the majority of solvated molecules having a slight decrease in charge. For strontiocenophanes, there is not much change that occurs due to solvation. Going from one-atom to two-atom bridging, regardless of whether it is carbon or silicon, slightly increases the charge of the metal. Overall, utilizing LMA can quantitatively display the differences in bridging motifs, solvation, and even substituents on the Cp ring, which change the stiffness of the Cp–M–Cp angle, as well as the charge of the metal.

To further elucidate the Cp–M–Cp interaction and the effects of the bridging motifs, $\nabla^2(\rho(r))$ maps were created within the Cp–M–Cp plane. The Laplacian contour plots of complexes **1a**, **1a-dme**, **1c**, **1c-(thf)$_2$**, **1e**, **1f**, **2d**, and **3c** are shown in Fig. 9(b). The Laplacian contour plots of selected complexes can be found in the ESI† (Fig. S2 and S3). Going from the non-solvated **1a** structure to the solvated **1a-dme** structure does not change the distribution of the Laplacian very much around the bridging motif and the ring structures. However, the effect of going from [1]carba-**1a** to [1]sila-**1c** bridging motifs is evident with the difference in the distribution of the Laplacian. In **1a**, there is local electron density distribution (charge concentration, indicated by the red dashed lines) between the bonds of the bridging motifs, whereas in **1c**, there is significantly greater charge depletion (indicated by the blue solid lines) around the silicon atom compared to the carbon atom. Going from the non-solvated **1c** to the solvated **1c-(thf)$_2$** structures, there is also a change in the Laplacian distribution, most likely due to the non-covalent interactions that are occurring between the solvent (THF) and the Cp rings. The difference in the contour map is also apparent going from [1]carba- to [2]carba-bridging motifs, with there being more charge concentrations occurring between the bonds in the bridging motif (**1e**). As seen before when changing from carbon to silicon, having a [2]sila-bridging motif (**1f**) allows for greater charge depletion around the silicon atoms, with the charge concentration occurring between the two silicon atoms. Finally, for **2d** and **3c**, the Laplacian of the electronic density is very similar to that of the [2]carba magnesocenophane (**1e**), with the only difference coming from the metal, with **2d** having more charge concentrations around its metal center, and **3c** having even more charge concentrations. Overall, the electronic density shows that the metal–oxygen bond is of electrostatic character, while the contour maps display the differences between

bridging motifs and metal centers, giving a more detailed insight into the electronic structure of the *ansa*-metallocene structures investigated.

Bent *versus* linear metallocenes

To further see the effects that the bridging motifs have on the *ansa*-metallocene structures, four metallocene compounds (labeled as **A**–**D**, see the ESI,† Fig. S1) were investigated (with the structures taken from a previous computational investigation from Pal *et al.*)[30] for comparison of the magnesocenophane and calcocenophane structures. There are three linear structures, $MgCp_2$ (**A**), $MgCp^*_2$ (**B**), and $CaCp_2$ (**C**), with one bent structure, $CaCp^*_2$ (**D**). Comparing the local force constants k^a (M–Cp) of the magnesocenophanes with the corresponding metallocene complex **A** (1.680 mdyn/Å), it appears that the [1]carba/[1]sila magnesocenophanes have a weaker Mg–Cp bond (with a corresponding slightly longer Mg–Cp bond length), whereas the [2]carba/[2]-sila have a stronger Mg–Cp bond (except for the THF-solvated **1d-thf** complex). However, for **B** (1.789 mdyn/Å), all the magnesocenophanes have a weaker Mg–Cp bond than the metallocene $MgCp^*_2$ (**B**), most likely this is due to the methylated substituents on the Cp ring. For structure **C** which has a force constant of 1.439 mdyn/Å, the structures that have a stronger Ca–Cp bond are **2d**, **2f**, **2g**, and **2h**. For structure **D**, the only structure that has the Cp* ring motif is **2b**, which has a weaker Ca–Cp bond, most likely due to the amide group attached to the calcium atom. Again, the effect of a solvent decreases the bond strength, where the weaker M–Cp bonds compared to the metallocene counterparts come from (i) single-bridged carbon, silicon, and phosphorus (from **2b**) motifs and (ii) THF or DME solvated structures, drastically affecting the strength of the M–Cp bond. Interestingly, the $CaCp^*_2$ (**D**) bond angle (155.1°) is much greater than all of the calcocenophanes, showing that the angle of the metallocene can be drastically affected if an *ansa*-motif is attached to it.

Conclusions

In this investigation, we have applied LMA as a quantitative bond strength for metal–π rings to 37 *ansa*-metallocene structures with group 2 metals ranging from non-solvated to solvated structures with donor solvents (THF and DME) and with different interannular motifs (carba- or sila-motifs with either single or double bridges). We first studied the overall effect of the M–Cp bond strength as one goes down the periodic table from Mg through Sr and confirmed that the M–Cp bond lengths from Mg to Sr increase; however, the local force constant does not drastically decrease, displaying that the strength of the M–Cp bond(s) is not dependent solely on the nature of the metal, but also dependent on the stability that is provided by the bridging motifs. We then studied the differences between non-solvated structures and solvated structures (which are usually characterized experimentally) utilizing the M–Cp bond strength, Cp–M–Cp angles, NBO charge of the metal, and Cp–M–Cp angle stiffness. Our findings indicate that the donor solvent makes a drastic change in the strength of the M–Cp bond and the stiffness of the Cp–M–Cp angle, mainly, that the coordination of the solvent inserted into the *ansa*-metallocenes drastically decreases the strength of the M–Cp bond and the stiffness of the Cp–M–Cp angle compared to its non-solvated counterpart. Furthermore, when investigating the metal–oxygen bond strengths between THF and DME solvents, it was discovered that DME has weaker metal–oxygen bonds than THF. Also, LMA was able to capture the ability to measure stiffness amongst different bridging motifs. These trends indicate that the silicon bridging atom(s), specifically the [2]sila-bridging motif, greatly increases the Cp–M–Cp angle. This would indicate that the silicon atom would be the best for transmetalation reactions since it decreases the bond strength and increases the bond angle for it to be more easily replaceable with its transition metal counterpart. To further investigate the electronic structure of the *ansa*-metallocene structures, QTAIM analysis was performed to calculate the energy density of the metal–oxygen bond and the Laplacian of the electronic density, which further supported the effects of solvated *ansa*-metallocenes and the nature of the bridging motifs. Comparing the linear/bent metallocene complexes, we see the general effect that the *ansa* interannular motif has on the strength of the M–Cp bond, as well as the effect of solvation, generally decreasing the bond strength. Overall, utilizing a robust computational tool set and including LMA can allow those who are interested in characterizing structures such as *ansa*-metallocenes a more efficient and quantitative way to calculate metal–π bond strengths, solvent effects, and effects of bridging motifs.

Conflicts of interest

There are no conflicts to declare.

Acknowledgements

This work was supported by the National Science Foundation, Grant CHE 2102461, and the National Science Foundation Graduate Research Fellowship Program under Grant No. DGE-2034834. We thank the Center for Research Computation at SMU for providing generous high–performance computational resources. J. J. A. thanks Barbara M. T. C. Peluzo for their valuable insight into the Laplacian plots.

Notes and references

1 L. Resconi, L. Cavallo, A. Fait and F. Piemontesi, *Chem. Rev.*, 2000, **100**, 1253–1345.
2 M. Bochmann, *J. Organomet. Chem.*, 2004, **689**, 3982–3998.
3 M. V. Kharlamova and C. Kramberger, *Nanomaterials*, 2023, **13**, 774.
4 Z. Xin, Y.-R. Wang, Y. Chen, L.-Z. Dong and Y.-Q. Lan, *Nano Energy*, 2020, **67**, 104233.

5 Y. Zhao, X. Xu, Y. Wang, T. Liu, H. Li, Y. Zhang, L. Wang, X. Wang, S. Zhao and Y. Luo, *RSC Adv.*, 2022, **12**, 21111–21121.
6 V. M. Rayón and G. Frenking, *Chem. – Eur. J.*, 2002, **8**, 4963.
7 E. D. Brady, S. C. Chmely, K. C. Jayaratne, T. P. Hanusa and V. G. Y. Jr., *Organometallics*, 2008, **27**, 1612–1616.
8 S. J. Grabowski and R. D. Parra, *Molecules*, 2022, **27**, 6269.
9 S. Baguli, S. Mondal, C. Mandal, S. Goswami and D. Mukherjee, *Chem. – Asian J.*, 2022, e202100962.
10 P. J. Shapiro, *Coord. Chem. Rev.*, 2002, **231**, 67–81.
11 C. E. Zachmanoglou, A. Docrat, B. M. Bridgewater, G. Parkin, C. G. Brandow, J. E. Bercaw, C. N. Jardine, M. Lyall, J. C. Green and J. B. Keister, *J. Am. Chem. Soc.*, 2002, **124**, 9525–9546.
12 A. Cicolella, E. Romano, V. Barone, C. D. Rosa and G. Talarico, *Organometallics*, 2022, **41**, 3872–3883.
13 M. A. Bau, S. Wiesler, S. L. Younas and J. Streuff, *Chem. – Eur. J.*, 2019, **25**, 10531–10545.
14 M. Kessler, S. Hansen, C. Godemann, A. Spannenberg and T. Beweries, *Chem. – Eur. J.*, 2013, **19**, 6350–6357.
15 L. Wirtz, W. Haider, V. Huch, M. Zimmer and A. Schäfer, *Chem. – Eur. J.*, 2020, **26**, 6171–6184.
16 H.-R. H. Damrau, A. Geyer, M.-H. Prosenc, A. Weeber, F. Schaper and H.-H. Brintzinger, *J. Organomet. Chem.*, 1998, **553**, 331–343.
17 P. Perrotin, B. Twamley and P. J. Shapiro, *Acta Crystallogr., Sect. E: Struct. Rep. Online*, 2007, **63**, m1277–m1278.
18 W. Haider, V. Huch and A. Schäfer, *Dalton Trans.*, 2018, **47**, 10425–10428.
19 M. Rieckhoff, U. Pieper, D. Stalke and F. T. Edelmann, *Angew. Chem. Int. Ed. Engl.*, 1993, **32**, 1079–1081.
20 K. M. Kane, P. J. Shapiro, A. Vji, R. Cubbon and A. L. Rheingold, *Organometallics*, 1997, **16**, 4567–4571.
21 G. J. Matare, K. M. Kane, P. J. Shapiro and A. Vij, *J. Chem. Crystallogr.*, 1998, **28**, 731–734.
22 B. Twamley, G. J. Matare, P. J. Shapiro and A. Vij, *Acta Crystallogr., Sect. E: Struct. Rep. Online*, 2001, **57**, m402–m403.
23 P.-J. Sinnema, B. Höhn, R. L. Hubbard, P. J. Shapiro, B. Twamley, A. Blumenfeld and A. Vij, *Organometallics*, 2002, **21**, 182–191.
24 L. Wirtz and A. Schäfer, *Chem. – Eur. J.*, 2021, **21**, 1219–1230.
25 H.-R. H. Damrau, A. Geyer, M.-H. Prosenc, A. Weeber, F. Schaper and H.-H. Brintzinger, *J. Organomet. Chem.*, 1998, **553**, 331–343.
26 L. Wirtz, J. Lambert, B. Morgenstern and A. Schäfer, *Organometallics*, 2021, **40**, 2108–2117.
27 L. Wirtz, K. Y. Ghulam, B. Morgenstern and A. Schäfer, *ChemCatChem*, 2022, **14**, e202201007.
28 E. Kraka, M. Quintano, H. W. L. Force, J. J. Antonio and M. Freindorf, *J. Phys. Chem. A*, 2022, **126**, 8781–8900.
29 E. Kraka, W. Zou and Y. Tao, *Wiley Interdiscip. Rev.: Comput. Mol. Sci.*, 2020, **10**, 1480.
30 R. Pal, S. Mebs, M. W. Shi, D. Jayatilaka, J. M. Krzeszczakowska, L. A. Malaspina, M. Wiecko, P. Luger, M. Hesse, Y.-S. Chen, J. Beckmann and S. Grabowsky, *Inorg. Chem.*, 2018, **57**, 4906–4920.
31 Z. Konkoli and D. Cremer, *Int. J. Quantum Chem.*, 1998, **67**, 1–9.
32 Z. Konkoli, J. A. Larsson and D. Cremer, *Int. J. Quantum Chem.*, 1998, **67**, 11–27.
33 E. B. Wilson, *J. Chem. Phys.*, 1941, **9**, 76–84.
34 J. D. Kelley and J. J. Leventhal, *Problems in Classical and Quantum Mechanics: Normal Modes and Coordinates*, Springer, 2017, pp. 95–117.
35 E. B. Wilson, J. C. Decius and P. C. Cross, *Molecular Vibrations: The Theory of Infrared and Raman Vibrational Spectra*, McGraw-Hill, New York, 1955.
36 V. Barone, S. Alessandrini, M. Biczysko, J. R. Cheeseman, D. C. Clary, A. B. McCoy, R. J. DiRisio, F. Neese, M. Melosso and C. Puzzarini, *Nat. Rev. Methods Primers*, 2021, **1**, 38.
37 W. Zou, M. Freindorf, V. Oliveira, Y. Tao and E. Kraka, *Can. J. Chem.*, 2023, **101**, 616–632.
38 M. Z. Makos, W. Zou, M. Freindorf and E. Kraka, *Mol. Phys.*, 2020, e1768314.
39 B. M. T. C. Peluzo, M. Z. Makos, R. T. Moura Jr., M. Freindorf and E. Kraka, *Inorg. Chem.*, 2023, **62**, 12510–12524.
40 E. Kraka, J. J. Antonio and M. Freindorf, *Chem. Commun.*, 2023, **59**, 7151–7290.
41 J. J. Antonio and E. Kraka, *Biochemistry*, 2023, **62**, 2325–2337.
42 D. Cremer and E. Kraka, *Curr. Org. Chem.*, 2010, **14**, 1524–1560.
43 E. Kraka, J. A. Larsson and D. Cremer, *Computational Spectroscopy*, Wiley, New York, 2010, pp. 105–149.
44 A. A. A. Delgado, D. Sethio and E. Kraka, *Inorganics*, 2021, **9**, 1–18.
45 A. A. A. Delgado, D. Sethio, I. Munar, V. Aviyente and E. Kraka, *J. Chem. Phys.*, 2020, **153**, 1–11.
46 R. F. W. Bader, *Acc. Chem. Res.*, 1985, **18**, 9–15.
47 R. F. W. Bader, *Atoms in Molecules: A Quantum Theory*, Clarendon Press, Oxford, 1995.
48 P. Popelier, *Atoms in Molecules: An Introduction*, Prentice-Hall, Harlow, England, 2000.
49 D. Cremer and E. Kraka, *Angew. Chem., Int. Ed. Engl.*, 1984, **23**, 627–628.
50 D. Cremer and E. Kraka, *Croatica Chem. Acta*, 1984, **57**, 1259–1281.
51 E. Kraka and D. Cremer, *Theoretical Models of Chemical Bonding. The Concept of the Chemical Bond*, ed. Z. B. Maksic, Springer Verlag, Heidelberg, 1990, vol. 2, pp. 453–542.
52 E. Kraka and D. Cremer, *J. Mol. Struct. THEOCHEM*, 1992, **255**, 189–206.
53 A. D. Becke, *J. Chem. Phys.*, 1993, **98**, 5648.
54 C. Lee, W. Yang and R. G. Parr, *Phys. Rev. B: Condens. Matter Mater. Phys.*, 1988, **37**, 785–789.
55 S. Grimme, J. Antony, S. Ehrlich and H. Krieg, *J. Chem. Phys.*, 2010, **132**, 154104.
56 F. Weigend and R. Ahlrichs, *Phys. Chem. Chem. Phys.*, 2005, **7**, 3297–3305.
57 M. J. Frisch, G. W. Trucks, H. B. Schlegel, G. E. Scuseria, M. A. Robb, J. R. Cheeseman, G. Scalmani, V. Barone, G. A. Petersson, H. Nakatsuji, X. Li, M. Caricato, A. V. Marenich, J. Bloino, B. G. Janesko, R. Gomperts,

B. Mennucci, H. P. Hratchian, J. V. Ortiz, A. F. Izmaylov, J. L. Sonnenberg, D. Williams-Young, F. Ding, F. Lipparini, F. Egidi, J. Goings, B. Peng, A. Petrone, T. Henderson, D. Ranasinghe, V. G. Zakrzewski, J. Gao, N. Rega, G. Zheng, W. Liang, M. Hada, M. Ehara, K. Toyota, R. Fukuda, J. Hasegawa, M. Ishida, T. Nakajima, Y. Honda, O. Kitao, H. Nakai, T. Vreven, K. Throssell, J. A. Montgomery, Jr., J. E. Peralta, F. Ogliaro, M. J. Bearpark, J. J. Heyd, E. N. Brothers, K. N. Kudin, V. N. Staroverov, T. A. Keith, R. Kobayashi, J. Normand, K. Raghavachari, A. P. Rendell, J. C. Burant, S. S. Iyengar, J. Tomasi, M. Cossi, J. M. Millam, M. Klene, C. Adamo, R. Cammi, J. W. Ochterski, R. L. Martin, K. Morokuma, O. Farkas, J. B. Foresman and D. J. Fox, *Gaussian-16 Revision B.01*, 2016, Gaussian Inc., Wallingford CT.

58 W. Zou, R. Moura Jr., M. Quintano, F. Bodo, Y. Tao, M. Freindorf, M. Z. Makos, N. Verma, D. Cremer and E. Kraka, LModeA2023, Computational and Theoretical Chemistry Group (CATCO), Southern Methodist University: Dallas, TX, USA, 2023.

59 E. D. Glendening, J. K. Badenhoop, A. E. Reed, J. E. Carpenter, J. A. Bohmann, C. M. Morales, P. Karafiloglou, C. R. Landis and F. Weinhold, NBO 7.0, 2018, Theoretical Chemistry Institute, University of Wisconsin, Madison, WI.

60 T. A. Keith, *AIMAll (Version 19.10.12)*, 2019, TK Gristmill Software, Overland Park KS, USA.

61 T. Sergeieva, T. I. Demirer, A. Wuttke, R. A. Mata, A. Schäfer, G.-J. Linker and D. M. Andrada, *Phys. Chem. Chem. Phys.*, 2023, **25**, 20657.